Highly dispersed TiO$_2$ nanocrystals and WO$_3$ nanorods on reduced graphene oxide: Z-scheme photocatalysis system for accelerated photocatalytic water disinfection

Xiangkang Zeng[a], Zhouyou Wang[a], Gen Wang[a], Thomas R. Gengenbach[b], David T. McCarthy[c], Ana Deletic[c], Jiaguo Yu[d], Xiwang Zhang[a,*]

[a] Department of Chemical Engineering, Monash University, Clayton, VIC 3800, Australia
[b] CSIRO Manufacturing, Bayview Avenue, Clayton, VIC 3168, Australia
[c] Environmental and Public Health Microbiology Laboratory (EPHM Lab), Monash Infrastructure Research Institute, Department of Civil Engineering, Monash University, Clayton, VIC 3800, Australia
[d] State Key Laboratory of Advanced Technology for Materials Synthesis and Processing, Wuhan University of Technology, Wuhan 430070, P.R. China

ARTICLE INFO

ABSTRACT

Coupling TiO$_2$ with WO$_3$ to develop photocatalytic heterojunctions is one of the most widely used strategies to realize their superior photoactivity. However, the interfacial charge transfer in these heterojunctions is not efficient to achieve an optimized activity. For the first time, the present study reports a facile hydrolysis-hydrothermal approach, whereby ultradispersed TiO$_2$ nanocrystals and WO$_3$ nanorods are concurrently anchored onto reduced graphene oxide (rGO) and formed a novel Z-scheme heterojunction photocatalyst TiO$_2$/rGO/WO$_3$ (TRW). Transmission electron microscope (TEM), X-ray diffraction (XRD), X-ray photoelectron spectroscopy (XPS), UV–vis diffuse reflectance spectroscopy (UV–vis DRS) and photoluminescence spectra (PL) are employed to characterize TRW. Control experiments indicate that, in the synthesis process, glucose and the by-product sodium chloride from the hydrolysis reactions are critical for forming highly dispersed and uniform-sized TiO$_2$ nanocrystals and WO$_3$ nanorods. Compared with TiO$_2$/WO$_3$ nanocomposites, TRW shows enhanced activity for bacterial inactivation under simulated solar light. As confirmed by electrochemical characterizations and the reactive oxygen species, rGO in TRW suppresses the recombination of electron-hole pairs and boosts the O$_2$ reduction reactions during photocatalytic process. Z-scheme electron transfer in TRW is proposed based on surface redox reactions and XPS analysis after light irradiation. This study could provide a new clue for designing graphene-based heterojunction photocatalysts for environmental applications.

© 2017 Elsevier B.V. All rights reserved.

1. Introduction

Water is an essential element for life. However, microbial contamination in impaired water has always threatened the health of human beings [1]. Millions of people die from diseases caused by waterborne pathogens every year [2]. Therefore, efficient methods to control or prevent the spread of pathogenic microorganisms in water are urgently needed [3]. Although conventional technologies for water disinfection have been widely used to inactivate pathogens aiming to supply safe drinking water, such as chlorination, ozonation and ultraviolet (UV) irradiation, they are either chemically intensive forming carcinogenic disinfection by-products (DBPs) or energy intensive contributing to the global warming [2–4]. An important trend to develop alternative disinfection methods is to explore novel approaches which can affordably and robustly inactivate traditional and emerging pathogens, and meanwhile do not create new issues [5]. Recently, as an advanced "green" oxidation technology, photocatalytic water disinfection has attracted increasing attentions [6,7]. With solar light, the most abundant, free and renewable energy on the earth, moderate reactive oxygen species (ROS) generated from photoactivated semiconductors can effectively kill pathogens [6,8,9]. Therefore, photocatalysis represents an environment-friendly, cost-effective and efficient advanced oxidation process for water disinfection [10].

Among all the semiconductors, titanium dioxide (TiO$_2$) is the most popular photocatalyst and has exhibited great potential in

* Corresponding author.
  E-mail addresses: xiwang.zhang@monash.edu, zhangxiwang@gmail.com (X. Zhang).

water purification considering its non-toxicity, strong oxidizing ability, chemical stability and bulk availability [11]. However, the relatively wide bandgap, major absorption in the UV light, and fast recombination of electron−hole pairs limit the widespread usage of TiO_2 [12,13]. To overcome these crucial drawbacks, coupling TiO_2 with other semiconductors to construct heterojunction photocatalysts is one of the most widely used strategy [13]. Tungsten trioxide (WO_3), with a small bandgap of between 2.4 eV to 2.8 eV, is another important semiconductor which shows photocatalytic activity under visible light [14,15]. By now, some studies have been done to incorporate TiO_2 with WO_3 forming heterojunction TiO_2/WO_3 (TW) nanocomposites and the nanocomposites exhibited higher photocatalytic activity than TiO_2 or WO_3 alone [16–20]. Combining TiO_2 with tungsten oxide firstly extends the light adsorption of the nanocomposites to the visible or even near infrared regions [20]. More importantly, due to the staggered band levels of TiO_2 and WO_3, interfacial charge transfer between them could happen [13,19]. As a result, the separation and migration of photogenerated carriers are promoted by the internal field and the recombination of electron-hole pairs is reduced [13]. However, due to the mismatch in morphologies and crystal structures, the interaction between TiO_2 and WO_3 is usually very poor, limiting the interfacial charge transfer [21]. In addition, in TW nanocomposites, the electrons accumulated on WO_3 are unfavourable for forming $O_2^{\bullet-}$ since the bottom of conduction band of WO_3 is more positive than the redox potential of $O_2^{\bullet-}/O_2$ [22]. The surface redox reactions for producing ROS from separated electron-hole pairs are crucial to the bactericidal activity of a photocatalyst [6]. Therefore, toward constructing heterojunction photocatalysts with high performance for water disinfection, both high charge-separation efficiency and strong redox ability are desirable.

Artificial heterogeneous Z-scheme photocatalytic systems, which mimic the natural photosynthesis process, represent advanced photocatalysis and have been widely used for energy production and environmental recommendation [23]. Recently, Z-scheme photocatalysts such as CdS–WO_3, CdS–Au–TiO_2 and $NaNbO_3/WO_3$ have been reported and shown enhanced photocatalytic activities for CO_2 reduction and dye degradation, respectively [24–26]. Among all Z-scheme photocatalytic systems, all-solid-state Z-scheme photocatalysis has attracted increasing attentions due to its unique properties [27]. Most recently, reduced graphene oxide (rGO) has been proven to be an excellent solid electron mediator of the Z-scheme photocatalysis system for water splitting, shuttling photogenerated electrons from O_2-evolving photocatalyst to H_2-evolving photocatalyst [28,29]. These elaborate works provide us a hint, if TiO_2 and WO_3 are linked by conductive rGO nanosheets, fast interfacial electron transfer via rGO might be achieved. Moreover, rGO nanosheets in graphene-based nanocomposites have been demonstrated to be good co-catalysts which can promote the photocatalytic reduction of oxygen to hydrogen peroxide (H_2O_2) [30–32]. Given the vital roles of rGO as electron transfer mediator and O_2 reduction booster in the photocatalytic process, we hypothesize that heterojunction photocatalysts with highly dispersed TiO_2 and WO_3 nanocrystals concurrently deposited on rGO could show enhanced disinfection performance.

Although, either TiO_2 or WO_3 has been deposited on rGO forming TiO_2/rGO or WO_3/rGO nanocomposites in literature [31,33–35], no work has been done to concurrently anchor TiO_2 and WO_3 nanocrystals onto rGO at separated positions, forming an all-solid-state Z-scheme photocatalyst. Herein, we report for the first time the synthesis of ultradispersed TiO_2 nanocrystals and WO_3 nanorods co-decorated rGO (TRW) by a facile hydrolysis-hydrothermal method. As illustrated in Fig. 1, the hydrolysis of titanium chloride and sodium tungstates in GO aqueous suspension deposits amorphous TiO_2 and tungstic acid (H_2WO_4) on GO. With the following hydrothermal treatment at 180 °C for 12 h, GO

is reduced to rGO, meanwhile amorphous TiO_2 and H_2WO_4 are converted to TiO_2 nanocrystals and WO_3 nanorods, respectively. Photocatalytic water disinfection tests show the TRW has superior performance than the binary TW counterparts. Moreover, the photocatalytic generation of ROS by TRW and TW are monitored to explain the enhanced bacterial inactivation performance. Finally, the possible electron transfer and surface redox reactions in TRW photocatalysis are proposed to explore the reaction mechanism.

2. Experimental

2.1. Chemicals and materials

Graphite flakes (+100 mesh), titanium chloride ($TiCl_4$), sodium tungstate dehydrate ($Na_2WO_4 \cdot 2H_2O$), $KMnO_4$, 2, 3-Bis (2-methoxy-4-nitro-5-sulfophenyl)-2H-tetrazolium-5-carboxanilide (XTT) sodium salt, 2, 9-dimethyl- 1, 10-phenanthroline (DMP), terephthalic acid and dialysis tubing cellulose membrane were purchased from Sigma-Aldrich used as-received. Other reagents, including ethanol, D-(+)-glucose, H_2SO_4, HCl, $NaNO_3$, sodium phosphates and H_2O_2 were of analytical grade and purchased from Merk Australia. Ultrapure water from Milli-Q system was used for all experiments.

2.2. Photocatalysts synthesis

Graphene oxide (GO) was prepared from commercial graphite flakes according to the modified Hummer's method [36]. The purified GO aqueous suspension (3 mg mL^{-1}, pH = 3.5) was stored in a fridge (4 °C) and used for further experiments. To synthesis TRW nanocomposite, GO suspension (30 mL, 1 mg mL^{-1}) was diluted with ultrapure water and kept ultrasonic treatment for 30 mins. Then D-(+)-glucose (10 mg) was added to the GO suspension and kept stirring for 5 mins. After that, $TiCl_4$ (50 μL) liquid was dropwise added to the mixture with vigorous magnetic stirring in ice bath. After 30 mins, Na_2WO_4 solution (0.92 mL, 0.5 M) was added to the mixture. The pH of solution was then adjust to around 2.0 with HCl (1 M) and kept stirring for another 1 h. Finally, the mixture was transferred into a Teflon-sealed autoclave (50 mL) and maintained at 180 °C for 12 h. The resultant black suspension was filtrated though 0.22 μm filter (Merck Millipore) and washed with ethanol solution (95%) and ultrapure water for several times, then resuspend in DI water. To remove the impurity, the suspension was put in a dialysis tubing cellulose membrane (molecular weight cut-off = 14,000) and dialysis against ultrapure water for one week. The purified photocatalysts were used for further experiments. TRW sample (control) was also prepared without glucose following the same process. To prepare binary TiO_2/WO_3 (termed as TW) photocatalyst, Na_2WO_4 solution (0.92 mL, 0.5 M) was mixed with ultrapure water (30 mL) and then $TiCl_4$ (50 μL) liquid was dropwise added to the mixture. The WO_3/rGO (termed as WR) photocatalyst was prepared from the mixture of Na_2WO_4 solution (0.92 mL, 0.5 M) and GO suspension (30 mL, 1 mg mL^{-1}). The pH of all mixed solution was adjusted to 2.0 with HCl (1 M). They were then treated with the same procedure of the aforementioned hydrothermal reaction.

2.3. Characterization

The morphologies of photocatalysts were characterized by transmission electron microscopy (TEM, FEI Tecnai G2 T20 TWIN and FEI Tecnai G2 F20 TWIN). X-ray diffraction (XRD) patterns of samples were collected in the range of 5–80° using a Rigaku Miniflex 600 X-ray diffract meter with Cu Kα radiation. X-ray photoelectron spectroscopy (XPS) analysis was performed
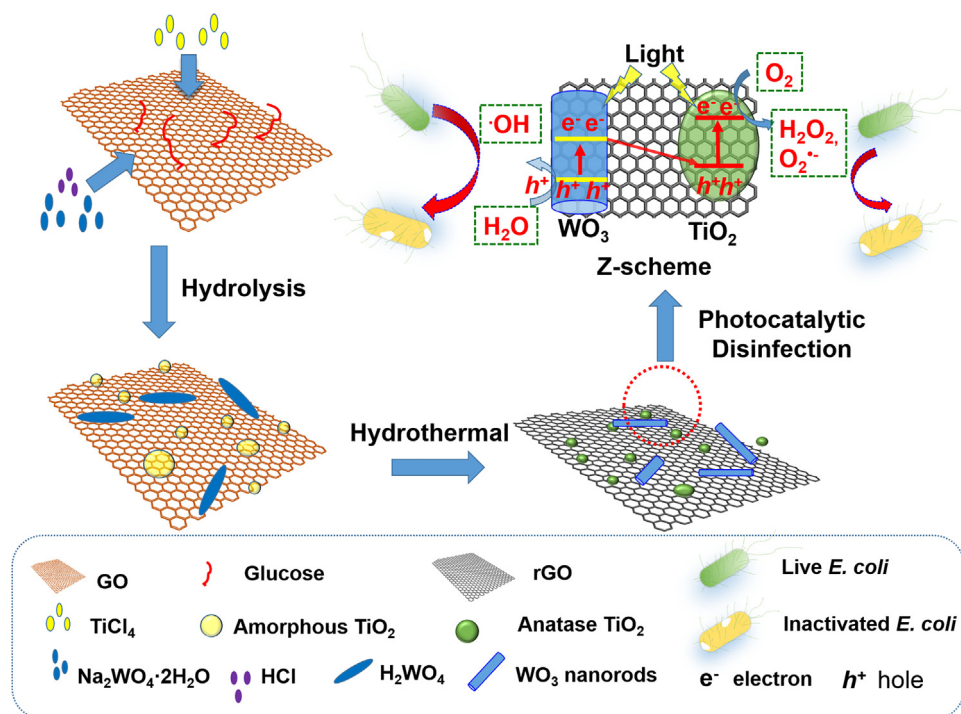
Fig. 1. Illustration of the synthesis of TRW and its application as Z-scheme photocatalysis system for water disinfection.

using an AXIS Nova spectrometer (Kratos Analytical Inc., Manchester, UK) with a monochromated Al Kα source at a power of 180 W (15 kV 12 mA) and the standard aperture (analysis area: 0.3 mm × 0.7 mm). Survey spectra were acquired at a pass energy of 160 eV. To obtain more detailed information about chemical structure, oxidation states etc., high resolution spectra were recorded from individual peaks at 20 eV pass energy (yielding a typical peak width for polymers of <0.9 eV). Each specimen was analysed at an emission angle of 0° as measured from the surface normal. Assuming typical values for the electron attenuation length of relevant photoelectrons the XPS analysis depth (from which 95% of the detected signal originates) ranges between 5 and 10 nm for a flat surface. UV–vis diffuse reflectance spectra (DRS) of photocatalysts were analysed by UV-2600 UV–vis Spectrophotometers (Shimadzu) with BaSO$_4$ as the internal reflectance standard. Photoluminescence (PL) spectra were obtained on an F-7000 fluorescence spectrophotometer (Hitachi) with the excitation wavelength λ at 280 nm.

2.4. Photocatalytic bacterial inactivation

Photocatalytic water disinfection performance of each catalyst was evaluated by the inactivation of gram-negative bacteria *Escherichia coli* (*E. coli* ATCC 11775). Typically, a single colony of *E. coli* was placed in Luria Bertani (LB) medium (10 mL) in a shaking air bath (37 °C), overnight. In the next morning, this culture (0.2 mL) was transferred to fresh LB medium (10 mL) and incubated until its optical density at 600 nm reached 0.5. The bacterial cells in the media were harvested by centrifugation (8000 rpm for 10 min), washed twice and then diluted with sterile phosphate buffer (PB 0.1 M, pH 7.0) to around 2×10^3 colony forming units/mL (CFU/ml). The prepared *E. coli* suspension (30 mL) buffer was then mixed with powdered photocatalyst (3 mg) and stirred at 300 rpm for 10 mins before light irradiation (non-irradiated controls were kept in the dark). A 200 W arc Mercury-Xenon research lamp (Newport) with AM 1.5 air filter was used as a simulated solar light source. At the given time intervals (i.e. 0, 20, 40, 60 and 80 mins), samples (1 mL)

were taken from the suspension buffer and remained at 4 °C for no more than 2 h before plating. The suspension (0.1 mL, undiluted, four replicates) was spread onto LB agar plates and incubated at 37 °C for 18 h to form viable colony units. The bacterial inactivation rate was calculated as $N/N_0 \times 100\%$ where N and N_0 are the bacterial concentration of samples taken at certain time and before light irradiation, respectively. To test the reusability of TRW, after one batch of disinfection experiment, the photocatalyst in the suspension was collected by filtration through a sterilized filter (0.22 μm, Merck Millipore), washed with DI water, and then resuspend in the *E. coli* suspension (30 mL) for repeated photocatalytic disinfection. Five cycles of photocatalytic disinfection by TRW were done.

2.5. TEM images of E. coli cells

For TEM images of *E. coli* cells, *E. coli* suspension (5 mL, 10^8 CFU/ml) was mixed with the photocatalyst (0.5 mg) and treated with light irradiation for 90 mins. The pellets of cells were collected together with the settled catalysts after the suspension was centrifuged at 8000 rpm (10 min). Untreated *E. coli* were also collected and used as a control at the same time. The bacterial pellets were then treated by a serial of steps (fixing, dehydrating, polymerization and staining) for imaging as described in detail in our previous work [37].

2.6. Probing reactive oxygen species

ROS produced in photocatalytic system with and without light irradiation were measured in the same buffer containing the same amount of photocatalysts except without *E. coli* cells. Superoxide anion was measured with XTT (0.1 mM) and the formed XTT-formazan was measured by absorbance at 470 nm [38]. Hydrogen peroxide was determined by a colorimetric method using copper (II) ions and DMP at 454 nm [39]. Hydroxyl radical was detected with the terephthalic acid solution using the fluorescence technique [40]. During photocatalytic process, 3 mL of the suspension was taken at certain irradiated time and filtered through a 0.22 μm

Millipore filter to remove the photocatalysts. The filtrated were analysed by UV-2600 UV–vis Spectrophotometers (Shimadzu) or F-7000 fluorescence spectrophotometer (Hitachi) for absorbance or fluorescence measurement.

2.7. Electrochemical characterizations

All electrochemical characterizations were carried out on a three-electrode cell on a CHI 660E workstation (CH Instruments, USA). The working electrodes were prepared by depositing photocatalyst aqueous ink (0.2 mL, 1 mg/mL) onto the cleaned FTO glass electrode (3 cm × 1 cm).The film electrode was then dried at 60 °C for 12 h to make it firmly attached with FTO glass. Platinum wire and Ag/AgCl (saturated KCl) electrode were used as counter electrode reference electrode, respectively. Transient photocurrent responses for the electrodes were measured under 1.0 V bias vs. Ag/AgCl in phosphate buffer (0.1 M, pH 7.0). Electrochemical impedance spectra (EIS) were measured in the same electrolyte by applying 5 mv alternative signal versus the reference electrode over the frequency range of 1 MHz–0.1 Hz. For electrochemical O_2 reduction tests, the electrolyte solution was purged with high-purity N_2 or O_2 gas.

3. Results and discussion

3.1. Synthesis and characterization of photocatalysts

Fig. 2(a–b) shows representative transmission electron microscopy (TEM) images of TRW, in which highly dispersed nanoparticles are deposited on the surface of rGO nanosheets. High-resolution TEM (HRTEM) images of TRW (Fig. 2c–d) indicate that nanosized materials with two different morphologies coexist on rGO. One is nanoparticles with a size around 10 nm and the other is nanorods which are around 5 nm in diameter and 20–30 nm in length. The lattice fringe spacing of 0.235 nm of the nanoparticles (Fig. 2c) is in agreement with the (004) atomic planes of the anatase
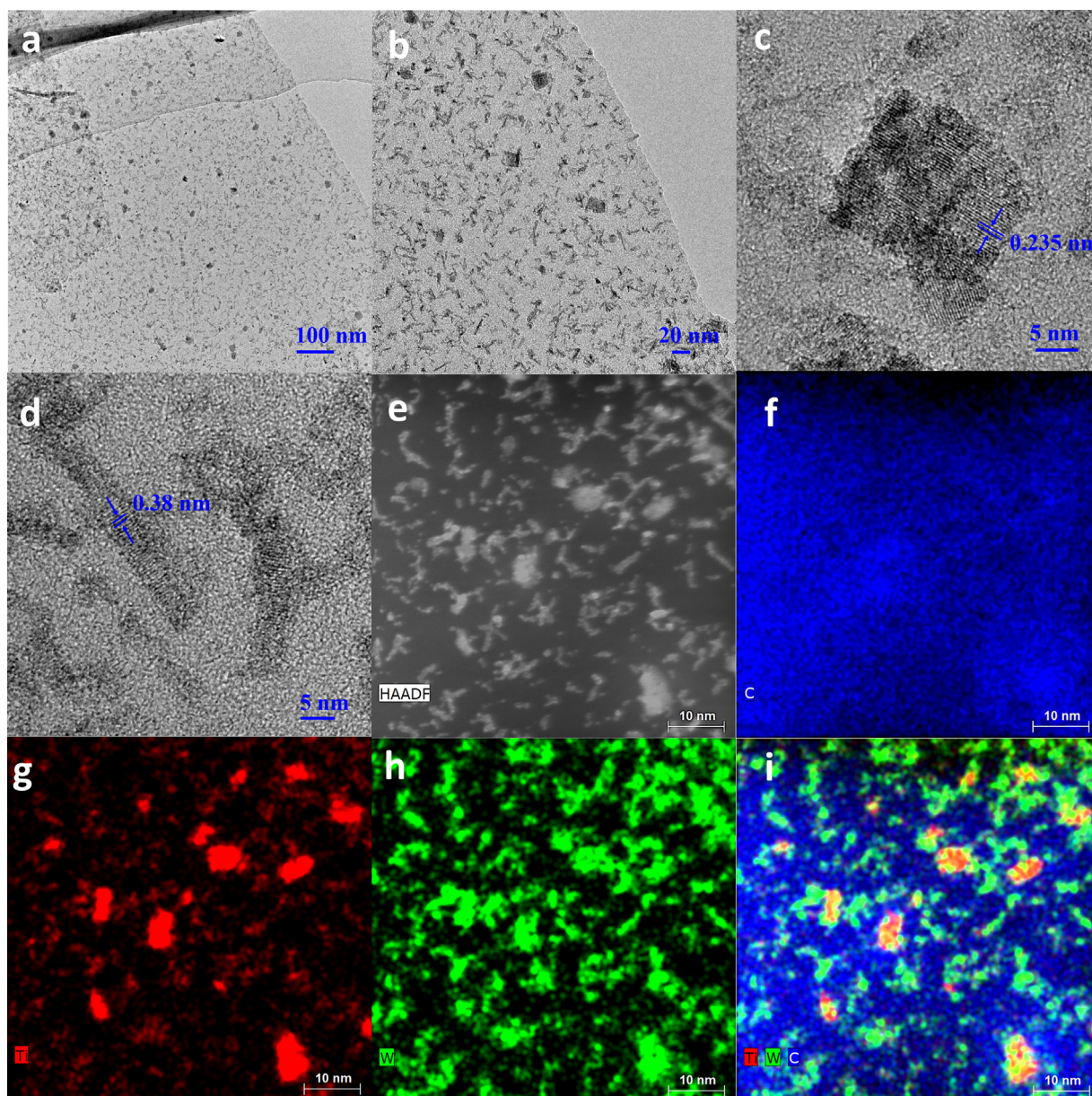

Fig. 2. TEM (a–b) and HRTEM (c–d) images of TRW nanocomposites. High angle annular dark field (HAADF)-STEM image (e) and the corresponding Carbon (f), Titanium (g), Tungsten (h) and mergerd (i) elemental mapping images of TRW.

TiO$_2$, which suggests they are TiO$_2$ nanocrystals [41]. While the one dimensional (1D) nanorods have a lattice fringe spacing of 0.38 nm (Fig. 2d) which are corresponding to the (002) planes of WO$_3$ crystalline[42]. To further prove the co-existence of TiO$_2$ nanocrystals and WO$_3$ nanorods on rGO, energy-dispersive X-ray spectroscopy (EDX) mapping of TRW was performed (Fig. 2e–i). The elemental mapping image of TRW (Fig. 2f–i) clearly shows that TiO$_2$ nanocrystals and WO$_3$ nanorods are incorporated onto rGO surface at separated sites when comparing the titanium (Ti) elemental image with tungsten (W) elemental image.

X-ray diffraction (XRD) was conducted to investigate the crystal structure of TRW as shown in Fig. 3a. The samples (TW and GO) were also characterised for comparison. The typical peaks at 25.1°, 38.6°, 46.4° and 55.1° indicate TiO$_2$ nanocrystals in TW and TRW are crystallized in anatase phase (JCPDS No. 21-1272)[43]. While the diffraction peaks at 13.8°, 24.2° and 36.5° indicate that WO$_3$ nanorods in both nanocomposites are in hexagonal phase

(JCPDS no. 75-2187) [35]. Moreover, GO shows a typical diffraction peak at 9.8°. However, after the hydrothermal treatment, no apparent peaks associated with rGO in TRW was found, which may be ascribed to the possible overlap of its main diffraction peak at around 25° with the peak of anatase TiO$_2$ at 25.1° [44]. The light absorption ability of photocatalysts was greatly enhanced after embedding TiO$_2$ and WO$_3$ nanocrystals onto rGO surface. As shown in the inset of Fig. 3b, TW is light green while TRW sample is black. The improved light absorption ability of TRW is confirmed by its UV–vis diffuse reflectance spectrum, which shows much better absorption in visible light than those of GO and TW (Fig. 3b). X-ray photoelectron spectroscopy (XPS) was employed to study the surface composition and chemical states of the prepared samples. From the survey spectrum of GO, the typical XPS peaks in the C 1 s and O 1 s region agree well with those of GO. The elements detected in TW and TRW nanocomposites were C, O, Ti and W (Fig. 3c). The atomic concentrations of C, O, Ti and W were 31.86%, 48.14% 5.29%,
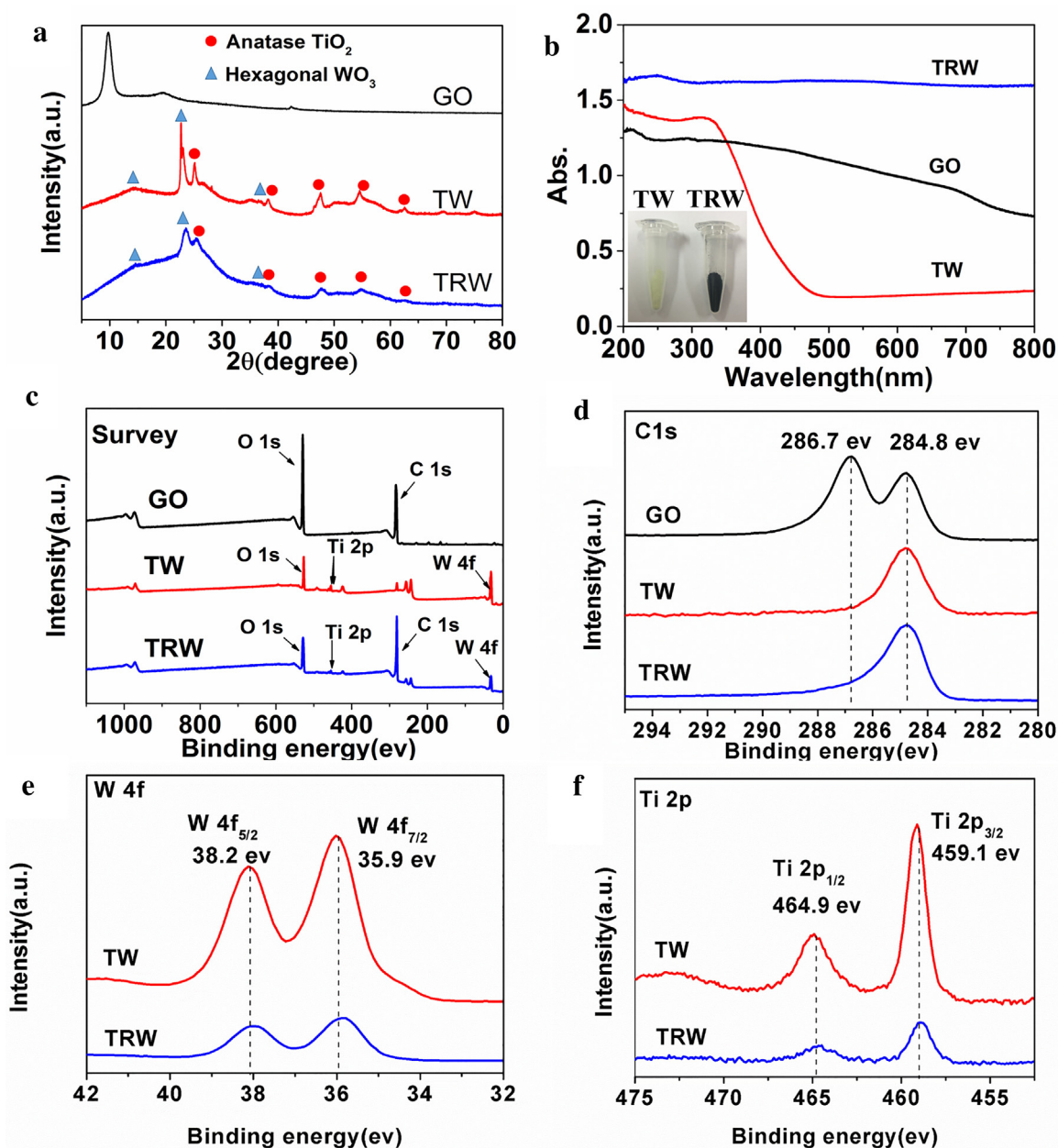

Fig. 3. XRD pattern of GO, TW and TRW (a); UV–vis diffuse reflectance spectra of GO, TW and TRW nanocomposites; the inset are photographs of freeze dried TW and TRW samples (b); XPS survey spectra of GO, TW and TRW(c); XPS high resolution spectra of C1s for GO, TW and TRW (d); W4f (e) and Ti2p (f) for TW and TRW.

13.4% and 76.98%, 20.7%, 0.76%, 1.54%, respectively for TW and TRW. The C 1s high resolution spectrum recorded on TW indicated C to be present mainly in the form of adsorbed aliphatic hydrocarbon contamination typically observed on metal and oxide surfaces (Fig. 3d). The equivalent spectrum of TRW displayed the characteristic asymmetric peak shape of graphitic carbon, specifically of rGO. It is compared in Fig. 3d with the C 1s recorded on GO prior to undergoing hydrothermal reaction. The latter is characteristic of unreduced GO, displaying strong peaks at 284.5–285 eV, representative of carbon not bonded to oxygen (sp^2/sp^3 carbon) and at approx. 286.7 eV (C–O, e.g. epoxy groups, hydroxyls) as well as some intensity at higher binding energy (C=O, O–C–O, O–C=O based groups). To a large extent the signal due to carbon-oxygen functional groups has disappeared in the case of TRW after hydrothermal reaction, verifying that GO was reduced to rGO after the hydrothermal reaction [45,46]. The high-resolution spectra of W4f for TW and TRW display a well-resolved doublet at 35.9 eV and 38.2 eV (Fig. 3e), indicating that W in both TW and TRW nanocomposites is in the +6 oxidation state [31,47]. Similarly, the Ti in both nanocomposites is in the +4 oxidation as verified by the Ti $2p_{3/2}$ and Ti $2p_{1/2}$ peaks at 459.1 eV and 464.9 eV, respectively, in the Ti2p spectra (Fig. 3f) [48]. Therefore, it can be further concluded that both TiO_2 and WO_3 are successfully deposited on rGO nanosheets.

To understand the formation of TRW nanocomposites, the morphologies of TRW were compared with those of TW nanocomposites prepared without GO. TEM images (Fig. 4a–b) show that the size and morphology of individual WO_3 nanorods and TiO_2 nanoparticles in TW are similar to those of TRW. However, WO_3 and TiO_2 in TW trend to aggregate forming large particles with a size of a few hundreds of nanometers. It has been known that the functional oxygen groups of GO are good anchoring sites for *in-situ* growth of nanoparticles [49]. Therefore, for TRW nanocomposites, during the hydrothermal reaction, the nucleus of nanocrystals can interconnect with GO nanosheet via its surface functional oxygen groups, and then well-dispersed WO_3 and TiO_2 particles were grown *in-situ* on these sites. Meanwhile, GO was reduced to rGO during the hydrothermal treatment. In this way, rGO in the final nanocomposites becomes a good scaffold for anchoring WO_3 and TiO_2 and prevent their aggregation.

In addition, glucose is crucial to the synthesis of TRW during the hydrothermal reaction. As shown in Fig. 4c–d, aggregated nanoparticles are formed in the absence of glucose. Due to the abundant hydroxyl groups, glucose molecules adsorb on TiO_2 and WO_3, controlling their growth on rGO and preventing the aggregation [33]. Therefore, glucose leads to the formation of well-dispersed TiO_2 and WO_3 nanocrystals on the rGO nanosheets. The result is in good agreement with our previous study, in which glucose was used as a dispersant for *in-situ* growth of highly-dispersed TiO_2 nanocrystals on rGO by a hydrothermal reaction [50].

Moreover, another interesting phenomenon is that $TiCl_4$, the precursor of TiO_2, plays an important role for the formation of 1D WO_3 nanorods in the hydrothermal reaction. Fig. 4e–f show non-uniform WO_3 nanorods with large size are formed when WR was prepared in the absence of $TiCl_4$. It has been reported that NaCl is a good agent to control the growth, dispersion and size of WO_3 nanorods as NaCl molecules can attach onto the certain crystal planes of WO_3 nucleus and weaken the interactions between two nanorods [35,42]. In our synthesis reaction system of TRW, sodium ion (Na^+) and chloride ion (Cl^-) are generated by the hydrolysis of the two precursors of WO_3 and TiO_2, sodium tungstates (Eq. (1)) and $TiCl_4$ (Eq. (2)), respectively. As a result, the generated NaCl led to the formation of uniform 1D WO_3 nanorods in the hydrothermal reaction. To summary, with GO as the scaffold, glucose and the by-product NaCl of the hydrolysis of two precursors as surfactants or shape-controlling agents, well-dispersed and uniform TiO_2

nanocrystals and WO_3 nanorods were *in-situ* deposited on rGO via the simple hydrolysis-hydrothermal reaction.

$$Na_2WO_4 + 2H^+ \rightarrow 2Na^+ + H_2WO_4 \qquad (1)$$

$$TiCl_4 + 2H_2O \rightarrow 4H^+ + TiO_2 + 4Cl^- \qquad (2)$$
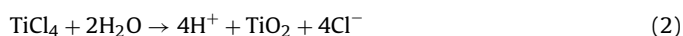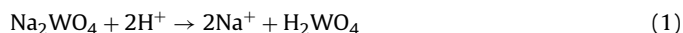
3.2. Photocatalytic water disinfection

The photocatalytic disinfection activity of TW, WR and TRW were investigated using *Escherichia coli* (*E. coli*) in aqueous phosphate-buffered (PB, 0.1 M, pH 7.0) solution. The inactivation of *E. coli* under dark condition (photocatalysts alone without light irradiation) and solar light irradiation alone (without photocatalysts) were also measured as control experiments. Under solar light irradiation alone without photocatalysts (Fig. 5a), few *E. coli* cells are inactivated. When the photocatalyst suspensions are irradiated by solar light, the number of viable *E. coli* colonies decreases with reaction time, and only few remain after 80 mins, suggesting that the photocatalyst suspension is efficient for inactivating *E. coli* (Fig. 5b). As illustrated in Fig. 5a, TRW slurry system reaches $97.3 \pm 3.8\%$ of *E. coli* inactivation within 80 mins while TW and WR only reaches $78.9 \pm 2.6\%$ and $45.5 \pm 3.7\%$, respectively. These results demonstrate that the photocatalytic *E. coli* inactivation activity of TRW composite is improved by concurrently embedding well-dispersed TiO_2 and WO_3 onto rGO. Moreover, TRW slurry system shows good performance for inactivating *E. coli* even under visible light (≥ 420 nm), achieving $67.5 \pm 7.9\%$ of *E. coli* inactivation within 80 mins (**Fig. S1**, Supplementary data). Furthermore, the stability and recyclability of TRW were also examined. The results evidenced that the photocatalytic activity of TRW did not decline significantly ($91.5 \pm 2.4\%$ of *E. coli* inactivation) after five cycles of *E. coli* inactivation under solar light irradiation, indicating its good reusability (Fig. S2, Supplementary data).

To understand the inactivation mechanism of *E. coli* cells, we studied the microstructure and morphology of *E. coli* cells before and after photocatalytic disinfection. Fig. 5c–d show the TEM images of untreated *E. coli* cells. Obviously, the untreated cells show uniform electron density in their TEM images, suggesting the membrane and wall structures are intact and well-preserved [51]. After photocatalytic inactivation by TW or TRW slurry, for many *E. coli* cells, a portion of their cell structure disappeared as indicated by the regions with light electron density in the TEM images (Fig. 5e–h). These results show the destruction to cell membranes and leakage of interior components by the photocatalytic inactivation process [9]. It has been reported that nanomaterials could be toxic to bacteria and inactivate cells through physical and/or chemical stress to the cell membrane when they are directly contacted [52,53]. However, the nanotoxicity of rGO, TiO_2 and WO_3 play negligible roles in disinfection in our system, as evidenced by the fact that only few cells were inactivated when they were mixed with TRW, WR and TW under dark conditions for 80 mins (**Fig. S3**, Supplementary data). This indicated that the ROS generated by TRW photocatalytic process, such as superoxide radicals ($O_2^{\bullet-}$), hydrogen peroxide (H_2O_2) and hydroxyl radicals ($^\bullet OH$), played the key roles in disinfection. When the ROS diffuse into the suspensions, they attack *E. coli* cells around the photocatalyst, causing alterations of cell permeability and/or even decomposition of the cell structure [9].

3.3. Photocatalytic generation of ROS

To gain an in-depth understanding of the role of rGO in the formation of ROS, the amount of ROS in both TRW and TW were measured. Firstly, the amount of $O_2^{\bullet-}$ was quantified by XTT method, in which $O_2^{\bullet-}$ reduces XTT to form XTT-formazan which has the specific absorption peak at 470 nm of XTT-formazan [38].
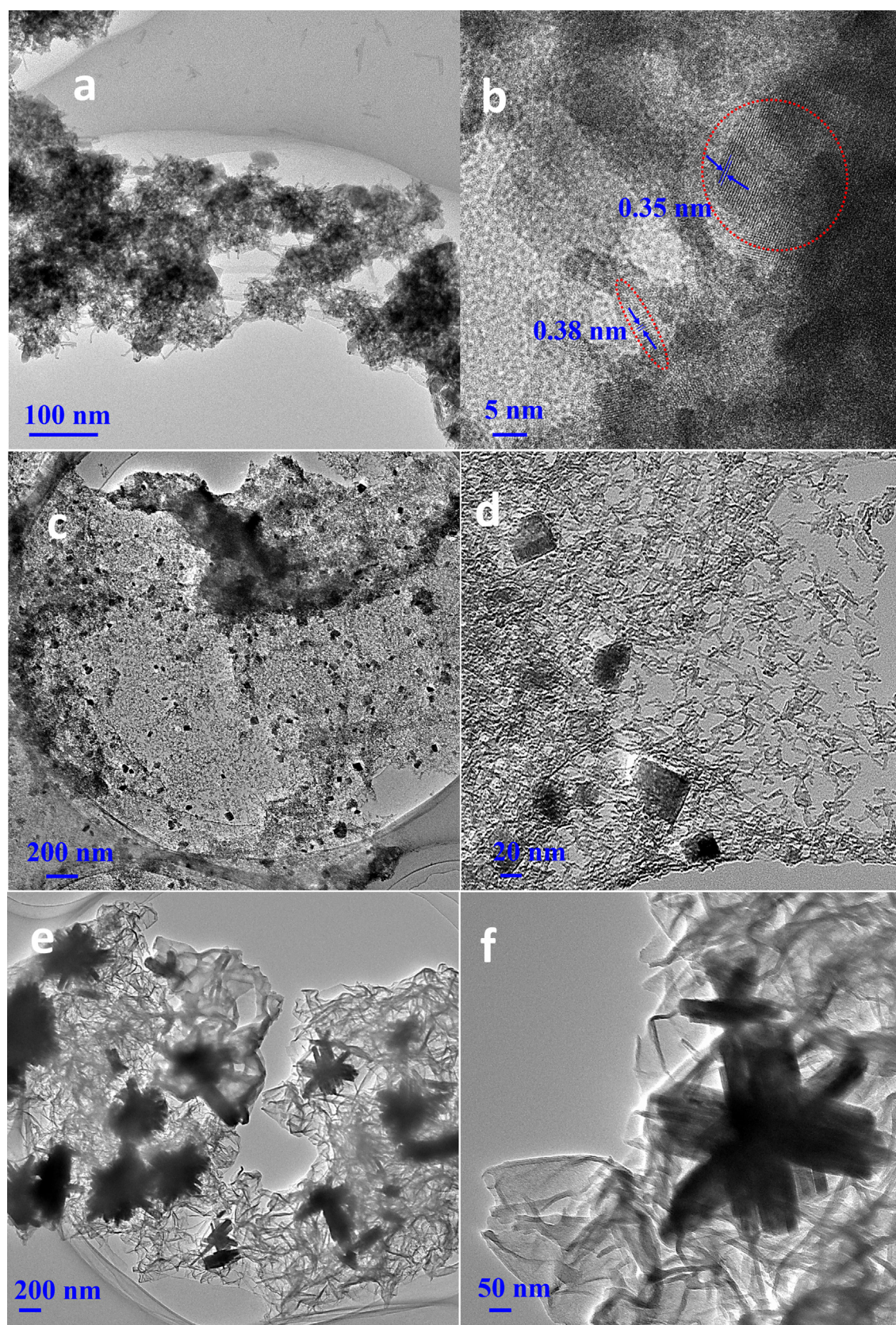
Fig. 4. TEM images of TW (a–b), TRW prepared without glucose (c–d) and WR nanocomposite prepared without $TiCl_4$ (e–f).
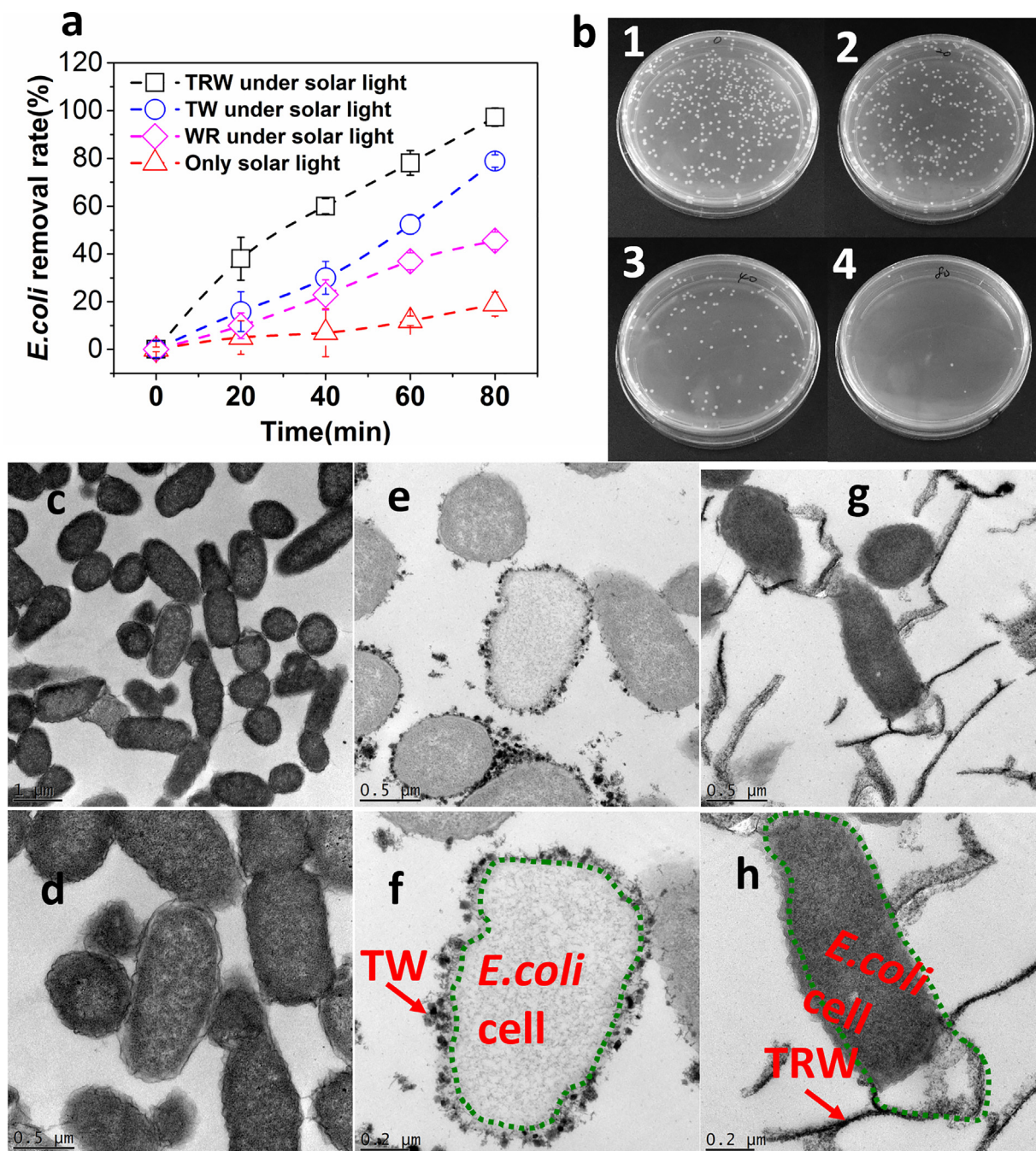
Fig. 5. (a) The inactivation of *E. coli* by TW, WR and TRW suspensions under simulated solar light; (b) Photographs of colonies formed *by E. coli* cells in water samples after treated by TRW suspensions with simulated solar light for 0 (b1), 20 (b2), 40 (b3) and 80 (b4) mins; (c–d) TEM images of untreated *E. coli* cells (control); (e–f) TEM images of *E. coli* cells treated by TW photocatalytic suspension; (g–h) TEM images of *E. coli* cells treated by TRW photocatalytic suspension.

Fig. 6a shows the concentration of the produced XTT-formanzan in TRW system is higher than that in TW within 90 mins, indicating that the generation of $O_2^{\bullet-}$ is enhanced in TRW system. In addition, the amount of H_2O_2 produced in TRW slurry is also much higher than that by TW (Fig. 6b). However, TW slurry shows better performance than TRW in term of $^{\bullet}OH$ production (Fig. 6c).

To determine which ROS plays the vital role for the inactivation of *E. coli* in TW and TRW slurry systems, scavengers for $^{\bullet}OH$, $O_2^{\bullet-}$ and H_2O_2 were added to the suspensions of photocatalysts. Control experiments showed the scavengers alone at the given concentration have no effect on the viability of *E. coli* within 60 mins (Fig. S4, Supplementary data). In TW photocatalytic system, the inactivation ratio of *E. coli* declined significantly with the scavenger for

$^{\bullet}OH$, suggesting that $^{\bullet}OH$ in the TW suspension plays an important role for disinfection (Fig. S5a, Supplementary data). While in TRW slurry, the addition of scavenger for H_2O_2 could almost completely inhibit the photocatalytic disinfection of *E. coli*, which indicates that H_2O_2 is mainly responsible for the inactivation of *E. coli* (Fig. S5b).

Despite $^{\bullet}OH$ has much higher oxidizing power than H_2O_2 and $O_2^{\bullet-}$, TRW suspension still shows better photocatalytic disinfection performance than TW. This is reasonable considering the different lifetimes of ROS. The lifetime of ROS determines the distance they can diffuse in the aqueous solutions. It is known that the lifetime of $^{\bullet}OH$ is only around 10 ns and it can only diffuse a very short distance (<20 nm) in aqueous solution within such shorter time [54]. TEM image of *E. coli* cells in Fig. 5f shows only a few TW nanocomposites
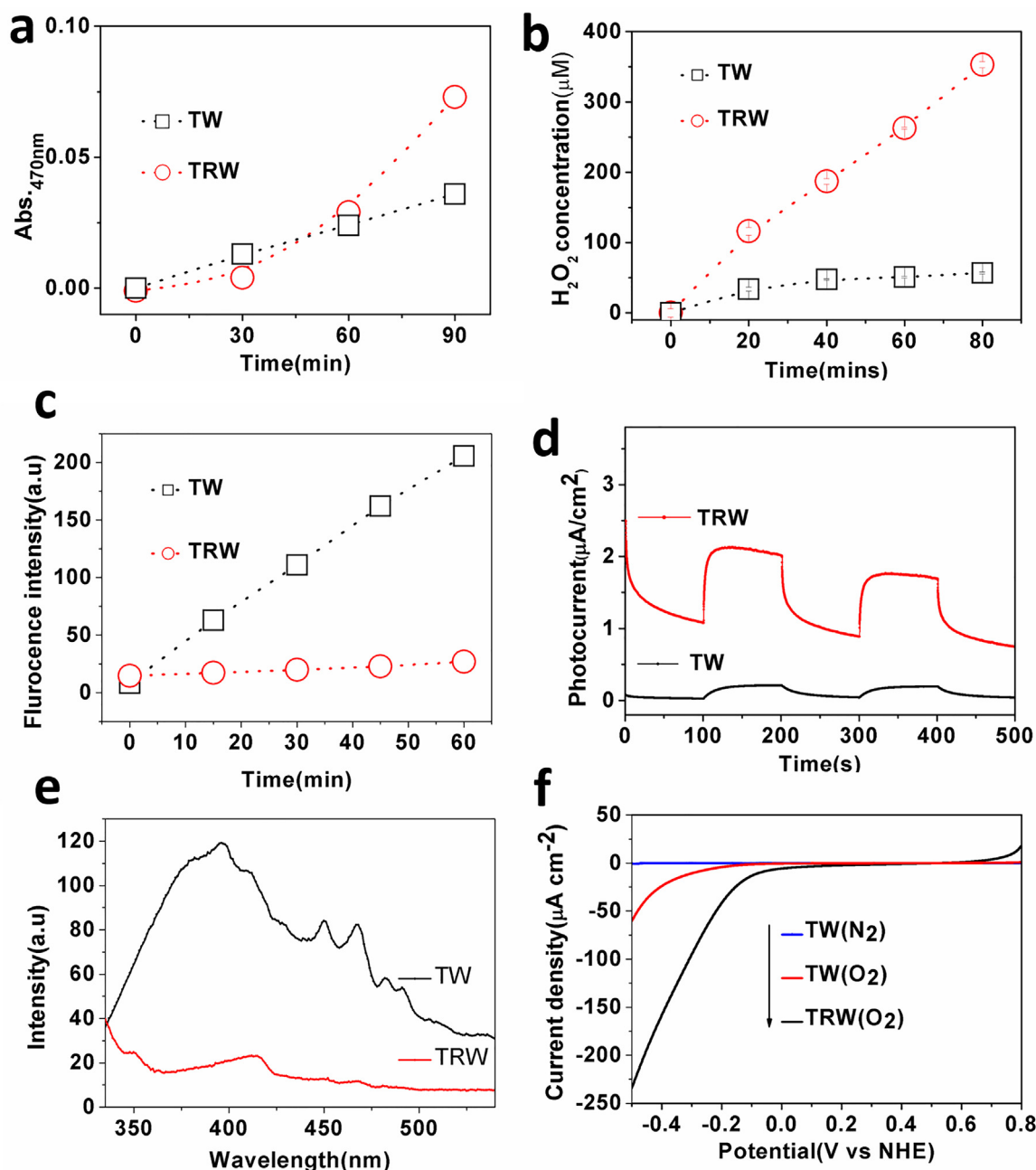
Fig. 6. Photocatalytic generation of $O_2^{\bullet-}$ (a), H_2O_2 (b) and $^{\bullet}OH$ (c) by TW and TRW suspensions under simulated solar light; (d) Photocurrent response curve of TW and TRW; (e) Photoluminescence (PL) spectra of TW and TRW; (f) Current-potential curves of the prepared TW and TRW electrodes in N_2 or O_2-saturated PB buffer solutions (0.1 M, pH = 7.0).

are closely attached on the surface of *E. coli*. It means that most of TW nanocomposites are not fully utilised. By contract, $O_2^{\bullet-}$ and H_2O_2 with relatively longer lifetimes can diffuse over long distance [54]. Even though TRW sheets partially wrapped the *E. coli* cells (Fig. 5h), the $O_2^{\bullet-}$ and H_2O_2 can still reach the *E. coli* cells. The results suggest that for photocatalytic disinfection relatively long-lived species ($O_2^{\bullet-}$ and H_2O_2) are more crucial than the short-life $^{\bullet}OH$.

3.4. Promoted charge separation and O_2 reduction reactions

Since photogenerated ROS are closely related with the lifetime of electron-hole pairs, the contribution of rGO to the separation of electron-hole pairs was investigated. Fig. 6d shows the photocurrent response of TW and TRW film electrodes. Obviously, the

photocurrent of TRW is around 4 times that of TW, which suggests the electron-hole separation efficiency of TRW is much higher[55]. To further study the electron-hole separation process, electrochemical impedance spectroscopy (EIS) was utilized to probe the separation efficiency of charge carrier. As shown by the EIS Nyquist plots (Fig. S6, Supplementary data), the arc radii of TRW is markedly smaller than that of TW, indicating lower resistance and improved charge transfer ability of TRW [56]. In addition, the photoluminescence (PL) spectra of TRW and TW are present in Fig. 6e. Clearly, after combined with rGO, the PL spectrum of TRW is completely quenched, suggesting that rGO effectively suppresses the recombination of charge in TRW nanocomposites [57].

Generally $O_2^{\bullet-}$ mainly comes from O_2 by one-electron reduction reaction at the surface of photocatalyst [58]. And for H_2O_2, it comes from either the two-electron reduction of O_2 or the combina-

tion of two •OH [32]. When 2-propanol (•OH scavenger) was added into the TRW suspension, the production of H_2O_2 was only declined slightly (Fig. S7, Supplementary data), suggesting that H_2O_2 is not from the combination of •OH but mainly from the two-electron reduction of O_2. Given a significant enhancement for the production of $O_2^{•-}$ and H_2O_2, it can be concluded that the surface O_2 reduction reactions in the TRW slurry system are promoted by rGO. This result is further confirmed by the electrochemical O_2 reduction on TRW and TW film electrodes. As shown in Fig. 6f, little current is observed when the electrodes are in the electrolyte saturated with N_2. While when the electrolyte buffer is saturated with O_2, obvious reduction currents were observed, indicating that O_2 reduction occurred on TRW and TW electrodes. Clearly, the one-electron reduction of O_2 (Eq. (3))[32] is improved in the presence of rGO as TRW shows a much larger reduction current at about −0.3 V vs. NHE than TW does. In addition, an obvious current at around 0.7 V vs. NHE contributed by the two-electron reduction of O_2 (Eq. (4))[32] occurred on TRW electrode but little current was observed for TW. Such results further indicate the O_2 reduction reactions in TRW are promoted by rGO.

$$O_2 + e^- \rightarrow O_2^{•-}, E^0_{NHE} = -0.33V \tag{3}$$

$$O_2 + 2H^+ + 2e^- \rightarrow H_2O_2, E^0_{NHE} = +0.695V \tag{4}$$
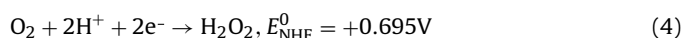
3.5. Photocatalytic mechanism of TRW: Z-scheme photocatalysis

The aforementioned results indicate that the migration of charge-carriers and surface redox reactions in TW and TRW photocatalysis systems are quite different. Herein, we discuss the possible charge transfer in TW and TRW based on their band levels and surface redox reactions. Fig. 7a shows the conduction band (CB) and the valence band (VB) levels of TiO_2 and WO_3 [22,59]. Since TiO_2 has a more negative CB level and less negative VB level than WO_3 does, photogenerated electrons are transferred from the CB of TiO_2 to WO_3, meanwhile, the holes in WO_3 will migrate to the VB of TiO_2 in TW nanocomposites (Fig. 7b). This heterojunction-type charge transfer process is further confirmed by the photochromism of TW suspension (turning to light blue as shown in Fig. S8, Supplementary data) [60]. Due to the charge transfer in TW, the photogenerated electrons and holes are accumulated in the CB of WO_3 and VB of TiO_2, respectively. As the CB level of WO_3 is more positive than the potential of $O_2^{•-}/O_2$, $O_2^{•-}$ could not be produced by WO_3. Moreover, the two-electron reduction of O_2 could be hindered due to the slow interfacial charge transfer. Therefore, the

concentrations of $O_2^{•-}$ and H_2O_2 in TW are very low. Since holes are accumulated on the VB of TiO_2 which is more positive than the redox potential of •OH/OH⁻ (+2.27 eV) [61], a large amount of •OH is produced in TW system.

However, in TRW system, considering the production of $O_2^{•-}$ and H_2O_2 is boosted while the formation of •OH is supressed, the charge transfer mode of TRW should be different from that of TW. Otherwise, if the heterojunction-type charge transfer mechanism is adopted, with rGO as an electron conduit, the photogenerated electrons would accumulate on WO_3 and holes would enrich on TiO_2. This would result in the improved production of •OH and declined formation of $O_2^{•-}$, which is inconsistent with the experimental results. We believe that Z-scheme electron transfer between WO_3 and TiO_2 happens on TRW. As proposed in Fig. 7c, with the migration of photogenerated electrons from CB of WO_3 to the VB of TiO_2 through conductive rGO, electrons and holes are accumulated in the CB of TiO_2 and the VB of WO_3, respectively. Since the CB of TiO_2 is more negative than the potentials of $O_2^{•-}/O_2$ and H_2O_2/O_2, both $O_2^{•-}$ and H_2O_2 can be produced by TiO_2. With rGO as the electron mediator in the Z-scheme transfer process, electrons enrich on TiO_2, which promotes the one-electron reduction of O_2 to $O_2^{•-}$. Moreover, previously, rGO in TiO_2/rGO and WO_3/rGO photocatalysts showed a superior cocatalytic behaviour for promoting two-electron reduction of dissolved O_2 to H_2O_2 [30–32]. As confirmed by the high concentration of H_2O_2 and electrochemical O_2 reduction data in TRW system (Fig. 6f), rGO plays another critical role of boosting the two-electron reduction of O_2 in TRW photocatalyst. For •OH, since holes from TiO_2 is recombined with electrons from WO_3, only holes in the VB of WO_3 are left for producing •OH. It has been reported that the formation rate of •OH on WO_3 is much slower than anatase TiO_2 [62]. Hence, TRW shows worse performance on the production of •OH than TW. To further prove the electron transfer in TRW is different from that in TW, XPS analysis was performed for TW and TRW samples after light irradiation for 1 h. As shown in **Fig. S9a** (Supplementary data), for TW treated by light irradiation for 1 h, a shoulder at 34–35 eV appears in the W4f high-resolution spectrum, indicating the partially reduction of W^{6+} to a lower valent W ion (W^{5+}) by the electrons accumulated on WO_3 [63]. By contrast, for TRW no shoulder or new peak belongs to lower valent W ion appears (**Fig. S9b**, Supplementary data) after light irradiation, indicating the photogenerated electrons are not accumulated on WO_3 in TRW. Such results further support electron
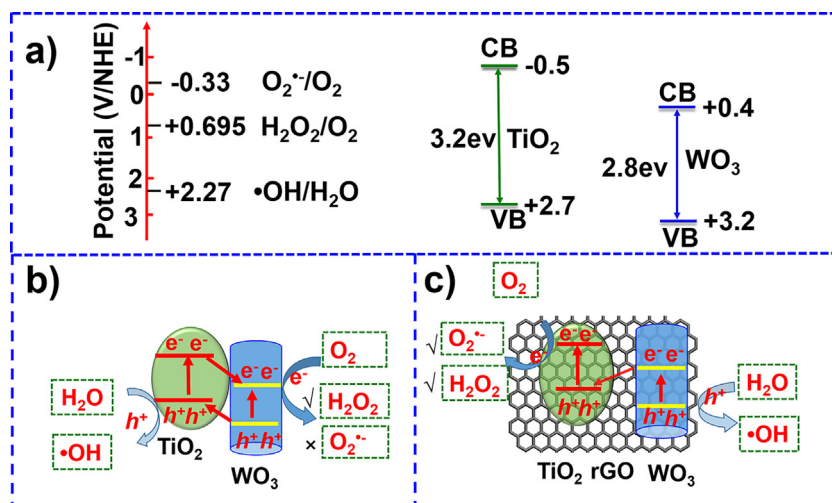

Fig. 7. Schematic diagram for describing the conduction band and valence band of TiO_2 and WO_3 (a); Heterojunction-type charge transfer and surface redox reactions for TW (b); Z-scheme charge transfer and surface redox reactions for TRW(c).

transfer mode in TRW nanocomposites should be the Z-scheme but not heterojunction-type.

4. Conclusions

Ternary nanocomposites with highly dispersed TiO_2 nanocrystals and WO_3 nanorods on rGO nanosheets were successfully synthesized via a facile hydrolysis-hydrothermal reaction. In this strategy, with GO as the scaffold, glucose and the by-product NaCl of the hydrolysis of two precursors as surfactants or shape-controlling agents, well-dispersed and uniform TiO_2 nanocrystals and WO_3 nanorods were *in-situ* deposited onto rGO. Compared with the binary TW nanocomposites, rGO in TRW promotes the interfacial electron transfer, which can effectively suppress the recombination of electron-hole pairs, and also boost the O_2 reduction reactions during photocatalytic process. With more relatively long-lived $O_2^{\bullet-}$ and H_2O_2 in the suspension, TRW showed enhanced photocatalytic performance on the inactivation of *E. coli*. Different from the conventional heterojunction-type charge transfer in TW, Z-scheme transfer process with rGO as electron mediator was confirmed in TRW. These results could provide a new clue for the construction of heterojunction photocatalysts for environmental applications.

Acknowledgements

Appendix A. Supplementary data

Supplementary data associated with this article can be found, in the online version, at http://dx.doi.org/10.1016/j.apcatb.2017.06.055.

References

[1] W.H. Organization, Emerging Issues in Water and Infectious Disease, World Health Organization, Geneva, 2003.
[2] R.P. Schwarzenbach, B.I. Escher, K. Fenner, T.B. Hofstetter, C.A. Johnson, U. Von Gunten, B. Wehrli, Science 313 (2006) 1072–1077.
[3] Q. Li, S. Mahendra, D.Y. Lyon, L. Brunet, M.V. Liga, D. Li, P.J. Alvarez, Water Res. 42 (2008) 4591–4602.
[4] D.L. Sedlak, U. von Gunten, Science 331 (2011) 42–43.
[5] M.A. Shannon, P.W. Bohn, M. Elimelech, J.G. Georgiadis, B.J. Marinas, A.M. Mayes, Nature 452 (2008) 301–310.
[6] C. Wei, W.Y. Lin, Z. Zainal, N.E. Williams, K. Zhu, A.P. Kruzic, R.L. Smith, K. Rajeshwar, Environ. Sci. Technol. 28 (1994) 934–938.
[7] M.R. Hoffmann, S.T. Martin, W. Choi, D.W. Bahnemann, Chem. Rev. 95 (1995) 69–96.
[8] P.-C. Maness, S. Smolinski, D.M. Blake, Z. Huang, E.J. Wolfrum, W.A. Jacoby, Appl. Environ. Microb. 65 (1999) 4094–4098.
[9] H.A. Foster, I.B. Ditta, S. Varghese, A. Steele, Appl. Microbiol. Biot. 90 (2011) 1847–1868.
[10] S. Malato, P. Fernández-Ibáñez, M. Maldonado, J. Blanco, W. Gernjak, Catal. Today 147 (2009) 1–59.
[11] M.D. Hernández-Alonso, F. Fresno, S. Suárez, J.M. Coronado, Energy Environ. Sci. 2 (2009) 1231–1257.
[12] M. Pelaez, N.T. Nolan, S.C. Pillai, M.K. Seery, P. Falaras, A.G. Kontos, P.S. Dunlop, J.W. Hamilton, J.A. Byrne, K. O'Shea, Appl. Catal. B Environ. 125 (2012) 331–349.
[13] H. Wang, L. Zhang, Z. Chen, J. Hu, S. Li, Z. Wang, J. Liu, X. Wang, Chem. Soc. Rev. 43 (2014) 5234–5244.
[14] Z.G. Zhao, M. Miyauchi, Angew. Chem. 120 (2008) 7159–7163.
[15] G.R. Bamwenda, H. Arakawa, Appl. Catal. A Gen. 210 (2001) 181–191.
[16] Y.T. Kwon, K.Y. Song, W.I. Lee, G.J. Choi, Y.R. Do, J. Catal. 191 (2000) 192–199.
[17] V. Puddu, R. Mokaya, G. Li Puma, Chem. Commun (2007) 4749–4751.
[18] J. Yang, X. Zhang, H. Liu, C. Wang, S. Liu, P. Sun, L. Wang, Y. Liu, Catal. Today 201 (2013) 195–202.
[19] M.V. Dozzi, S. Marzorati, M. Longhi, M. Coduri, L. Artiglia, E. Selli, Appl. Catal. B Environ. 186 (2016) 157–165.
[20] M. Yan, G. Li, C. Guo, W. Guo, D. Ding, S. Zhang, S. Liu, Nanoscale 8 (2016) 17828–17835.
[21] D. Zhao, C. Chen, C. Yu, W. Ma, J. Zhao, J. Phys. Chem C 113 (2009) 13160–13165.
[22] D. Tsukamoto, M. Ikeda, Y. Shiraishi, T. Hara, N. Ichikuni, S. Tanaka, T. Hirai, Chem. Eur. J 17 (2011) 9816–9824.
[23] H. Li, Y. Zhou, W. Tu, J. Ye, Z. Zou, Adv. Funct. Mater. 25 (2015) 998–1013.
[24] C. Shifu, J. Lei, T. Wenming, F. Xianliang, Dalton. Trans. 42 (2013) 10759–10768.
[25] J. Jin, J. Yu, D. Guo, C. Cui, W. Ho, Small 11 (2015) 5262–5271.
[26] H. Zhu, B. Yang, J. Xu, Z. Fu, M. Wen, T. Guo, S. Fu, J. Zuo, S. Zhang, Appl. Catal. B Environ. 90 (2009) 463–469.
[27] P. Zhou, J. Yu, M. Jaroniec, Adv. Mater. 26 (2014) 4920–4935.
[28] A. Iwase, Y.H. Ng, Y. Ishiguro, A. Kudo, R. Amal, J. Am. Chem. Soc. 133 (2011) 11054–11057.
[29] A. Iwase, S. Yoshino, T. Takayama, Y.H. Ng, R. Amal, A. Kudo, J. Am. Chem. Soc. 138 (2016) 10260–10264.
[30] X. Li, J. Yu, S. Wageh, A.A. Al-Ghamdi, J. Xie, Small 12 (2016) 6640–6696.
[31] B. Weng, J. Wu, N. Zhang, Y.-J. Xu, Langmuir 30 (2014) 5574–5584.
[32] G.-h. Moon, W. Kim, A.D. Bokare, N.-e. Sung, W. Choi, Energy Environ. Sci. 7 (2014) 4023–4028.
[33] B. Qiu, M. Xing, J. Zhang, J. Am. Chem. Soc. 136 (2014) 5852–5855.
[34] W. Li, F. Wang, S. Feng, J. Wang, Z. Sun, B. Li, Y. Li, J. Yang, A.A. Elzatahry, Y. Xia, J. Am. Chem. Soc. 135 (2013) 18300–18303.
[35] X. An, C.Y. Jimmy, Y. Wang, Y. Hu, X. Yu, G. Zhang, J. Mater. Chem. 22 (2012) 8525–8531.
[36] W.S. Hummers Jr., R.E. Offeman, J. Am. Chem. Soc. 80 (1958) 1339.
[37] X. Zeng, D.T. McCarthy, A. Deletic, X. Zhang, Adv. Funct. Mater. 25 (2015) 4344–4351.
[38] D.Y. Brunet, E.M. Lyon, P.J. Hotze, M.R. Alvarez, Environ. Sci. Technol. 43 (2009) 4355–4360.
[39] A.N. Baga, G.A. Johnson, N.B. Nazhat, R.A. Saadalla-Nazhat, Anal. Chim. Acta 204 (1988) 349–353.
[40] K.-I. Ishibashi, A. Fujishima, T. Watanabe, K. Hashimoto, Electrochem. Commun. 2 (2000) 207–210.
[41] F. Tian, Y. Zhang, J. Zhang, C. Pan, J. Phys. Chem. C 116 (2012) 7515–7519.
[42] J. Wang, E. Khoo, P.S. Lee, J. Ma, J. Phys. Chem. C 112 (2008) 14306–14312.
[43] J.S. Lee, K.H. You, C.B. Park, Adv. Mater. 24 (2012) 1084–1088.
[44] Y. Li, W. Gao, L. Ci, C. Wang, P.M. Ajayan, Carbon 48 (2010) 1124–1130.
[45] D.C. Marcano, D.V. Kosynkin, J.M. Berlin, A. Sinitskii, Z. Sun, A. Slesarev, L.B. Alemany, W. Lu, J.M. Tour, ACS Nano 4 (2010) 4806–4814.
[46] D. Long, W. Li, L. Ling, J. Miyawaki, I. Mochida, S.-H. Yoon, Langmuir 26 (2010) 16096–16102.
[47] F. Xie, L. Gong, X. Liu, Y. Tao, W. Zhang, S. Chen, H. Meng, J. Chen, J. Electron Spectrosc. 185 (2012) 112–118.
[48] B. Erdem, R.A. Hunsicker, G.W. Simmons, E.D. Sudol, V.L. Dimonie, M.S. El-Aasser, Langmuir 17 (2001) 2664–2669.
[49] H. Wang, J.T. Robinson, G. Diankov, H. Dai, J. Am. Chem. Soc. 132 (2010) 3270–3271.
[50] X. Zeng, Z. Wang, N. Meng, D.T. McCarthy, A. Deletic, J.-h. Pan, X. Zhang, Appl. Catal. B Environ. 202 (2017) 33–41.
[51] W.-R. Li, X.-B. Xie, Q.-S. Shi, H.-Y. Zeng, O.-Y. You-Sheng, Y.-B. Chen, Appl. Microbiol. Biot. 85 (2010) 1115–1122.
[52] Y. Tu, M. Lv, P. Xiu, T. Huynh, M. Zhang, M. Castelli, Z. Liu, Q. Huang, C. Fan, H. Fang, R. Zhou, Nat. Nanotechnol. 8 (2013) 594–601.
[53] C.A. Linkous, G.J. Carter, D.B. Locuson, A.J. Ouellette, D.K. Slattery, L.A. Smitha, Environ. Sci. Technol. 34 (2000) 4754–4758.
[54] R.W. Redmond, I.E. Kochevar, Photochem. Photobiol. 82 (2006) 1178–1186.
[55] M. Kong, Y. Li, X. Chen, T. Tian, P. Fang, F. Zheng, X. Zhao, J. Am. Chem. Soc. 133 (2011) 16414–16417.
[56] M. Adachi, M. Sakamoto, J. Jiu, Y. Ogata, S. Isoda, J. Phys. Chem. B 110 (2006) 13872–13880.
[57] J. Liu, H. Bai, Y. Wang, Z. Liu, X. Zhang, D.D. Sun, Adv. Funct. Mater. 20 (2010) 4175–4181.
[58] H. Sheng, H. Ji, W. Ma, C. Chen, J. Zhao, Angew. Chem. 125 (2013) 9868–9872.
[59] I.V. Lightcap, T.H. Kosel, P.V. Kamat, Nano Lett. 10 (2010) 577–583.
[60] T. He, Y. Ma, Y. Cao, X. Hu, H. Liu, G. Zhang, W. Yang, J. Yao, J. Phys. Chem. B 106 (2002) 12670–12676.
[61] A. Fujishima, T.N. Rao, D.A. Tryk, J. Photochem, Photobiol. C 1 (2000) 1–21.
[62] Q. Xiang, J. Yu, P.K. Wong, J. Colloid Interface Sci. 357 (2011) 163–167.
[63] T. Fleisch, G. Mains, J. Chem. Phys. 76 (1982) 780–786.